Smart Structures and Systems, *Vol. 24, No. 6 (2019) 709-721*
DOI: https://doi.org/10.12989/sss.2019.24.6.709

Vision-based dense displacement and strain estimation of miter gates with the performance evaluation using physics-based graphics models

Yasutaka Narazaki*[1], Vedhus Hoskere[1a], Brian A. Eick[1a], Matthew D. Smith[2b] and Billie F. Spencer[1c]

[1]*Department of Civi and Environmentall Engineering, University of Illinois at Urbana-Champaign, 205 N Mathews Ave, Urbana, IL 61801, USA*
[2]*Army Engineer Research and Development Center, 3909 Halls Ferry Rd., Vicksburg, Mississippi, 39180, USA*

(Received July 2, 2019, Revised August 25, 2019, Accepted August 29, 2019)

Abstract. This paper investigates the framework of vision-based dense displacement and strain measurement of miter gates with the approach for the quantitative evaluation of the expected performance. The proposed framework consists of the following steps: (i) Estimation of 3D displacement and strain from images before and after deformation (water-fill event), (ii) evaluation of the expected performance of the measurement, and (iii) selection of measurement setting with the highest expected accuracy. The framework first estimates the full-field optical flow between the images before and after water-fill event, and project the flow to the finite element (FE) model to estimate the 3D displacement and strain. Then, the expected displacement/strain estimation accuracy is evaluated at each node/element of the FE model. Finally, methods and measurement settings with the highest expected accuracy are selected to achieve the best results from the field measurement. A physics-based graphics model (PBGM) of miter gates of the Greenup Lock and Dam with the updated texturing step is used to simulate the vision-based measurements in a photo-realistic environment and evaluate the expected performance of different measurement plans (camera properties, camera placement, post-processing algorithms). The framework investigated in this paper can be used to analyze and optimize the performance of the measurement with different camera placement and post-processing steps prior to the field test.

Keywords: Miter gate; vision-based structural health monitoring; displacement and strain measurement; physics-based graphics model; optical flow, finite element analysis; graphics modeling

1. Introduction

Miter gates are essential components of the US inland waterways, stretching 25,000 miles and supporting about 14% of the domestic freight (American Society of Civil Engineers 2017). Appropriate monitoring and maintenance of miter gates are required for the uninterrupted safe operations of the waterways. Typical means of identifying structural conditions of miter gates are visual inspections, where human inspectors see the members of miter gates to identify damage (Greimann *et al.* 1992). The visual inspections tend to be costly and labor-intensive, sometimes taking gates out of service to perform underwater operations or dewatering of the lock chambers. To reduce the workload and economic loss incurred by such inspections, structural health monitoring platforms of miter gates based on sensor measurements have also been implemented. One of those platforms is the SMART Gate developed by the US Army Corps of Engineers. Using strain data from the SMART Gate, Eick *et al.* (2018) detect gaps at the quoin of a miter gate, where the slope of the strain-water level plot during the chamber water level change is used with the principal component analysis (PCA) to extract damage sensitive features. Hoskere *et al.* (2019) extends the research by applying the artificial neural networks to the slope features to detect the existence of quoin gaps and estimate the gap profiles. The behavior of the finite element model with the estimated gap profile is consistent with the strain measurement data from the SMART Gate.

The performance of the damage detection algorithms for miter gates is supported by the dense measurement of physical quantities, such as displacement and strain. Although the SMART Gate provides rich information from contact sensors (e.g., strain gages), the platform does not provide information of the entire surfaces of the structures. In consequence, damage detection at the parts with relatively less sensors tends to be challenging, and adding information from further dense measurement is beneficial to evaluate the entire structures.

Vision-based measurements are expected to supplement the data from contact sensors by increasing the spatial resolution of the measurement significantly with limited amount of cost (Spencer *et al.* 2019). Images can be obtained by non-contact measurement using cameras, and post-processing algorithms can be applied to estimate the displacement and strain at every location of the images. In the field of civil engineering, vision-based measurement has been investigated particularly for the structures where the

*Corresponding author, Ph.D. Student
E-mail: narazak2@illinois.edu
[a] Ph.D. Student
[b] Research Civil Engineer
[c] Professor

http://www.techno-press.com/journals/sss&subpage=7
ISSN: 1738-1584 (Print), 1738-1991 (Online)

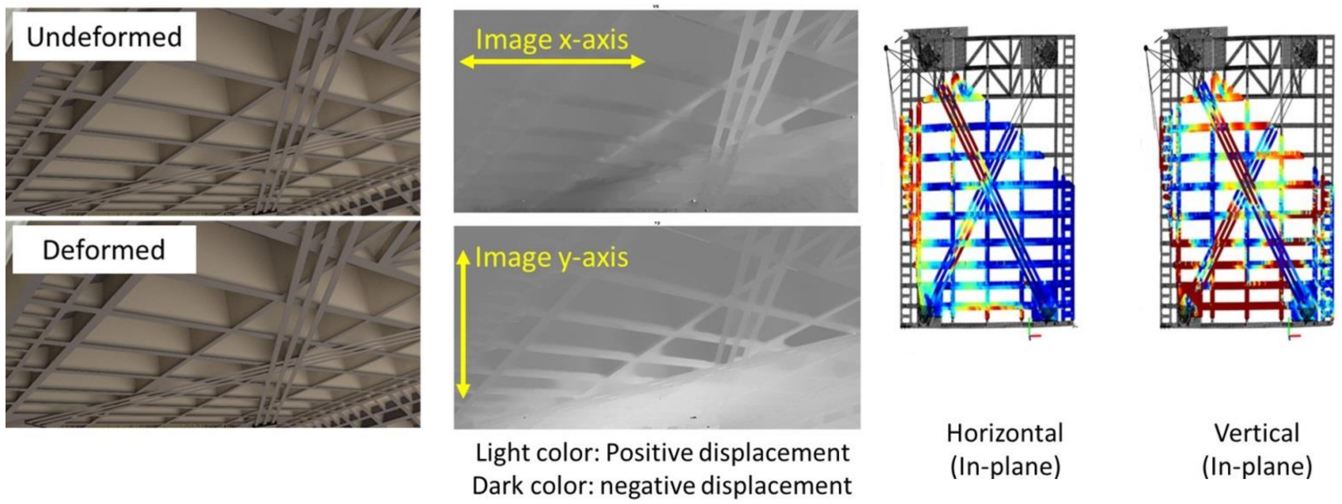

(a) Image collection (b) Optical flow estimation (c) 3D displacement/strain estimation with performance evaluation

Fig. 1 Steps of the proposed framework of 3D vision-based measurement

installation of contact sensors is difficult due to the accessibility issues and/or large size of the structure (Fukuda *et al.* 2013, Ye *et al.* 2013). The dense vision-based measurement has also been investigated to estimate the global deflection of bridges (Yoneyama *et al.* 2007, McCormick and Lord 2012) and strain fields of laboratory specimens (Ghorbani *et al.* 2015, Mahal *et al.* 2015). Visualization of structural behavior is another effective application of vision-based measurement, where small and almost invisible motions in video recordings are magnified by phase-based motion magnification technique (Wadhwa *et al.* 2013). Real-time digital image correlation for vibration measurement has been proposed and applied to bridge monitoring (Pan *et al*. 2016). Commercial software for the vision-based displacement and strain measurement has been developed (e.g., VIC-2D (*Correlated Solutions*), GOM Correlate (*GOM*)).

A challenge of applying the vision-based measurement in the field is that the accuracy of measurement is sensitive to factors such as camera intrinsic and extrinsic parameters, textures of target surface, and environmental conditions (e.g., lighting). Existing studies about accuracy evaluations thus limit their scopes by using specific combinations of cameras, specimens, and measurement settings (Hoult *et al.* 2013), or listing the factors affecting the accuracy qualitatively (Pan *et al.* 2009). However, cameras, lens, and/or target texture/environmental conditions of each field application are highly likely to be different from those investigated in the existing studies. Furthermore, unlike experimental applications, distance of cameras from target surfaces may not be close enough, or the camera orientations may be closely aligned with the direction of structural deformation, which makes the measurement challenging. Therefore, planning a measurement based on the predicted accuracy of the vision-based measurement before traveling to the site or validating the measurement results after collecting data is not straightforward.

To address the challenge, this paper investigates a framework of implementing vision-based dense 3D displacement and strain measurement of miter gates in the field, which has the following three components: (i) Estimation of 3D displacement and strain from images before and after deformation (water-fill event), (ii) evaluation of the expected accuracy of the measurement, and (iii) selection of measurement setting with the highest expected accuracy. The next section discusses the methodology employed in this framework, including the physics-based graphics model (PBGM) used to simulate and evaluate the vision-based measurements in a photo-realistic environment. Then, using the framework, a process of finding the best camera locations for the measurement of the miter gates of the Greenup lock and dam is demonstrated. The framework investigated in this paper can be used to analyze and optimize the performance of the measurement with different camera placement and post-processing steps prior to the field test.

2. Methodology

2.1 Overview of the proposed framework

Steps of the proposed framework are shown in Fig. 1. First, images before and after the deformation of the target structure are collected (Fig. 1(a)). Then, the full-field optical flow is computed between the images before and after the deformation (Fig. 1(b)). The optical flow is the 2D motion field in the image plane expressed in pixel unit, which is then converted to 3D displacement and strain field with physical units (e.g., inches). To address the challenge of estimating the expected performance of the measurement plans (camera properties, measurement locations etc.), the framework has an additional performance evaluation step. In this step, the entire process of the field test is simulated using the physics-based graphics model (PBGM), and the

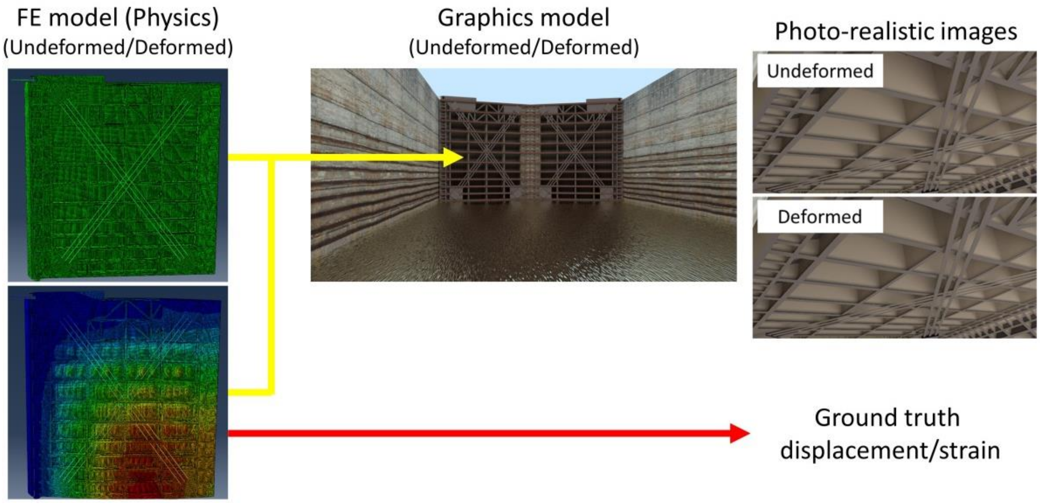

Fig. 2 Typical physics-based graphics modeling process

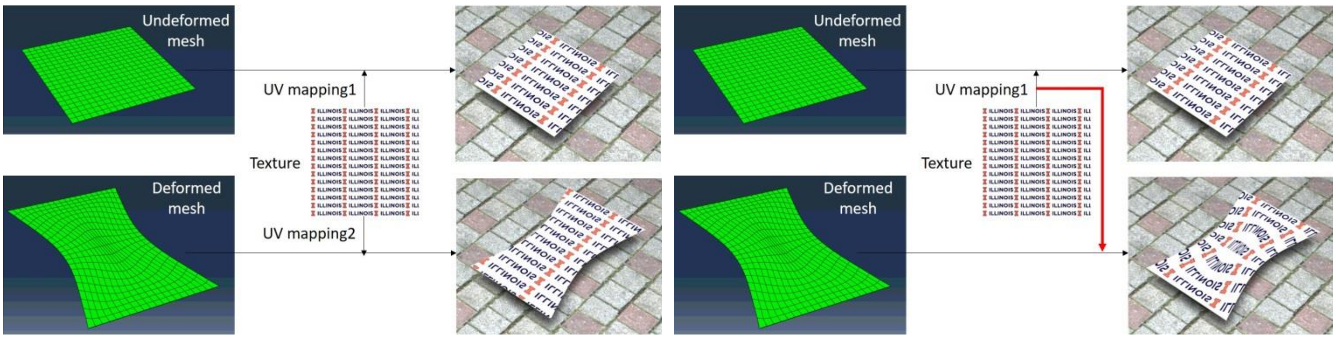

(a) (b)

Fig. 3 Texturing of physics-based graphics models (a) Naive approach, where the UV mapping is defined independently at each step (b) The approach of this research, where the UV mapping of the undeformed mesh is used consistently

estimated displacement and strain fields are compared with the ground truth values. The expected performance of the vision-based measurement algorithms can be visualized in the form of error maps shown in Fig. 1(c), where blue color shows low error (high accuracy) and red color shows high error (low accuracy). The maps of the expected performance can be used to compare different measurement settings (e.g., camera locations, post- processing algorithms) quantitatively to develop a measurement plan with optimized expected accuracy prior to the measurement in the field. The following sections describe each step of the framework in detail.

2.2 Physics-based graphics model for simulating vision-based measurement

The physics-based graphics model (PBGM) is a textured graphics model whose geometry and deformation are determined based on the physics-based analysis (i.e., finite element analysis) (Hoskere *et al*. 2019). Typical physics-based graphics modeling process is shown in Fig. 2. First, a finite element model of the target structure is created, and the structural behavior is estimated by applying realistic loads. The deformed and underformed mesh obtained by the finite element analysis can be represented by coordinates of nodes (vertices) and sets of vertices forming faces. The information of vertices and faces is then exported to a graphics engine and textured appropriately. This research uses Abaqus for the finite element analysis, and Abaqus-Python Scripting is used to read and export the mesh data. For graphics modeling, this research uses Blender with its Python API.

This synthetic environment can be used to simulate the entire measurement process by placing cameras at the planned locations/orientations and render images (intrinsic parameters such as focal length and resolutions can be set arbitrarily). Furthermore, the ground truth values for the measurement (displacement and strain fields) are available from the finite element analysis results, which can then be used to evaluate the expected performance of the measurement plan, including the selection of cameras/lens, camera locations/orientations, and post-processing algorithms.

One of the main differences of the PBGM used in this research from the PBGMs used previously by the authors (Hoskere *et al*. 2019, Narazaki *et al*. 2019) and other general synthetic datasets for the performance evaluation of optical flow algorithms (e.g. Baker *et al*. 2011) is the updated texturing step. During the physics-based graphics modeling, the target structure deforms according to the finite element analysis. If the structure is textured independently at each deformation stage, the mapping from the base image texture to the surface of the 3D mesh (UV mapping) does not stay consistent (Fig. 3(a)), posing difficulty in simulating surface displacement and strain measurement. To address this problem, this research stores the UV mapping for the undeformed mesh, and defines the UV mapping during subsequent steps such that the same vertex of the mesh is always mapped to the same point in the base image regardless of deformation. By implementing this updated texturing procedure using Blender-Python API, the surface texture of the PBGM can deform consistently with the underlying finite element analysis (Fig. 3(b)).

2.3 Full-field optical flow computation

Optical flow algorithms estimate the motion of each pixel of an image sequence by observing the spatial and temporal intensity change (Szeliski 2011). One of the simple yet effective methods for the optical flow estimation is the Lucas-Kanade algorithm (Lucas and Kanade 1981), which solves the optical flow constraint equation

$$I_x u + I_y v + I_t = 0 \tag{1}$$

where u, v are the motion of each pixel in image x and y axes, I_x, I_y, I_t are the partial derivatives of the image intensity with respect to the two image axes (x and y) and time t, respectively. Since this equation is underdetermined, the (weighted) least square solution of the optical flow constraint equation within a local patch is computed.

The optical flow estimation by the Lucas-Kanade algorithm faces challenge when (i) the optical flow constraint equation does not hold for reasons such as large motion, occlusion, and lighting changes, and/or (ii) image gradient is small (e.g. unique solution does not exist for uniform texture, or $I_x = I_y = 0$). (Barron *et al*. 1994). One of the approaches to get globally consistent optical flow estimation for such cases is to minimize an error function accumulated over the entire image (Horn and Schunck 1981)

$$\begin{aligned} &\int\int \left(I_x u + I_y v + I_t\right)^2 dx\, dy \\ &+\alpha \int\int \left\{\left(\frac{\partial u}{\partial x}\right)^2 + \left(\frac{\partial u}{\partial y}\right)^2 + \left(\frac{\partial v}{\partial x}\right)^2 + \left(\frac{\partial v}{\partial y}\right)^2\right\} dx\, dy \end{aligned} \tag{2}$$

The first double integral term corresponds to the optical flow constraint equation, and the second double integral term penalizes abrupt change of the optical flow, leading to smooth estimates even for the image parts where local method fails.

A hybrid of above two approaches has also been investigated to get smooth estimates where the local method fails, while preserving abrupt changes in the parts with high image gradient. Bruhn et al. (Bruhn *et al*. 2005) investigated the combined local-global (CLG) method by introducing a new integration scale parameter in the error function. The method combines the new error function with the spatiotemporal optimization applied in multiple resolutions to get accurate optical flow estimates for different magnitudes of motion. This research uses the MATLAB implementation of the CLG method by (Liu 2009).

Another approach for motion estimation particularly useful for large motion is template matching (Barron *et al*. 1994, Sutton *et al*. 2009, Pan *et al*. 2016). In template matching, parameterized motion (warping function) at each point in image is estimated by optimizing similarity measure (sum of square deviation, zero-mean normalized cross correlation, zero-mean normalized sum of squared difference etc.) between patches in the reference and target images. Iterative techniques, such as forward additive Gauss Newton (FA-GN) and inverse compositional Gauss Newton (IC-GN) algorithms are often employed to solve the optimization problem (Baker and Matthews 2004). Reliability-guided digital image correlation (RG-DIC) (Pan 2009) is one of the successful framework for estimating motion field by template matching: the method minimizes zero-mean normalized sum of square differences at each point iteratively, starting from the most reliable estimates of the neighbors. MATLAB implementation of the RG-DIC is available at (*Ncorr - Open source 2D digital image correlation MATLAB software*).

An example motion field estimation results by CLG approach and the RG-DIC are shown in Fig. 4, where the patch size of the RG-DIC algorithm is set to 43 pixel × 43 pixel after testing different values ranging from 22 × 22 to 172 × 172 pixels. The estimation by CLG approach is cleaner near the edges, compared to the blurred and/or inaccurate estimation by the RG-DIC. This is because the estimation from patches with the fixed shape and size is corrupted by the inclusion of multiple structural parts behaving differently. The estimation using patches with fixed size and shape suffers similar type of inaccuracy as the distance to the target structure changes. For example, motion near the bottom is smoothed too much in Fig. 4(b) compared to the CLG approach in Fig. 4(c). One of the advantages of the template matching approach over the CLG approach is its robustness to lighting change and deformation, since those effects are handled explicitly in the formulation. However, the effect of lighting change in the dataset investigated in this research is not significant, and the deformation of the gate is small throughout the measurement. Therefore, the CLG approach by (Liu 2009) is used in the subsequent sections.

2.4 Conversion of optical flow results into 3D displacement

Estimation of 3D displacement from the optical flow results in the (2D) image plane is a challenging problem because the solution is not unique mathematically. Any point on a ray originating from the camera center is mapped to the same point on the image plane and, without further assumptions, estimation of the 3D displacement from 2D optical flow data is impossible. A typical assumption to address the problem is to constrain the solution to the plane parallel to the image plane and neglect the motion perpendicular to the plane (e.g., Ye *et al*. 2013, Hoskere *et al*. 2018). Another possible approach is to assume the

(a) Images
Top: undeformed/Bottom: deformed

(b) RG-DIC (Ncorr)
Top: horizontal/Bottom: vertical

(c) CLG optical flow (Liu 2009)
Top: horizontal/Bottom: vertical

Fig. 4 Example motion field estimation results

direction of motion (e.g., vertical) and determine the magnitude of the displacement vector pointing to that direction (e.g., Pan *et al*. 2016)). When the assumptions are valid, these approaches have shown successful results. However, finding valid assumptions is not straightforward when the displacement field of the miter gate is estimated, because of the complexity of the displacement field.

This research considers two assumptions to convert the optical flow results into 3D displacement. The first assumption is that the displacement is in the horizontal plane, neglecting the vertical displacement (an approach similar to (Pan *et al*. 2016). The rationale for this assumption is the actual loading mechanism of the miter gates: deformation is caused by the water level difference between the upstream and downstream sides. This assumption can be interpreted as identifying the mapping from the 2D optical flow results to 3D displacement vectors in a subspace spanned by the two horizontal basis vectors.

The second assumption seeks for the better selection of the basis vectors to define appropriate subspaces adaptively. The key idea is to use the displacement obtained by the finite element analysis as an approximation of the displacement of the target structure. As shown in Fig. 5, the first basis vector is taken in the direction of the displacement obtained by the finite element analysis. Then, considering that the optical flow does not capture the motion on the ray connecting the camera center and the target point, a vector perpendicular to the ray and the first basis vector is selected as the second basis vector. Finally, a vector perpendicular to the first and second basis vectors is taken as the third basis vector. Using the basis vectors defined adaptively at each nodal location, the optical flow results are mapped to the 3D displacement vector in the subspaces spanned by the first two basis vectors. This assumption can take advantage of the prior knowledge about the complex structural behavior obtained by the finite element analysis.

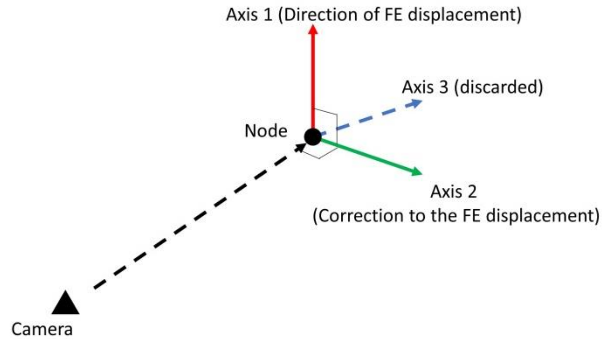

Fig. 5 Adaptive basis assumption

After determining the assumption (basis vectors), the 3D displacement vectors at the nodal locations of the target structure can be computed by solving

$$\tilde{x}_{\mathrm{im}} = \mathrm{P}\tilde{X}_{\mathrm{world}} \tag{3}$$

where $\tilde{x}_{\mathrm{im}} = (x_{\mathrm{im}}, y_{\mathrm{im}}, 1)^{\mathrm{T}}$ is the nodal location of the deformed structure in the image expressed in the homogeneous coordinate, P is the 3×4 camera calibration matrix, and $\tilde{X}_{\mathrm{world}} = (X_{\mathrm{world}}, Y_{\mathrm{world}}, Z_{\mathrm{world}}, 1)^{\mathrm{T}}$ is the unknown 3D location of the deformed structure in the homogeneous coordinate. Using the basis vectors (v_1, v_2) determined by the assumption, $\tilde{X}_{\mathrm{world}}$ can be rewritten as

$$\tilde{X}_{\mathrm{world}} = \tilde{X}^0_{\mathrm{world}} + \begin{bmatrix} v_1 & v_2 \end{bmatrix} \begin{bmatrix} c_1 \\ c_2 \end{bmatrix} \tag{4}$$

where $\tilde{X}^0_{\mathrm{world}}$ is the nodal location of the undeformed structure, and c_1, c_2 are the unknown linear combination coefficients. The linear combination coefficients can now be identified by the simple algebra, and the 3D displacement is obtained by

$$\begin{bmatrix} v_1 & v_2 \end{bmatrix} \begin{bmatrix} c_1 \\ c_2 \end{bmatrix} \tag{5}$$

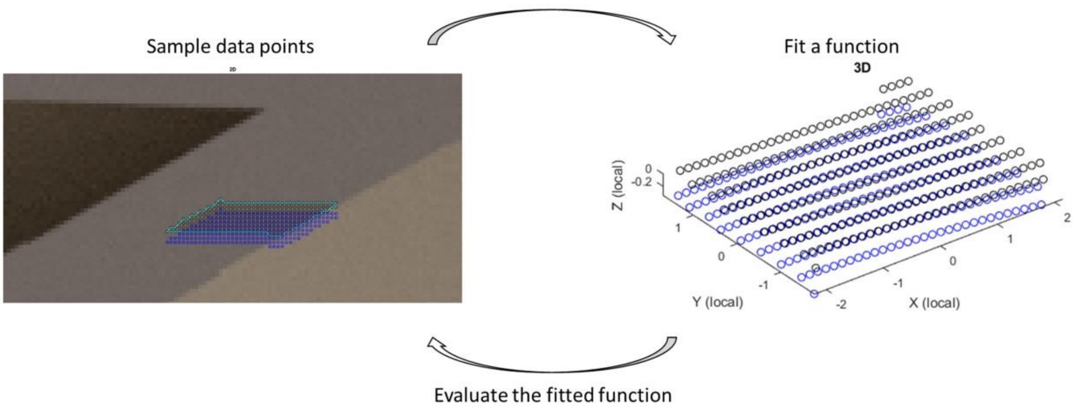

Fig. 6 Strain estimation steps. (left) Patch generation, (left to right) Fitting analytical functions to the displacement field in the patch, (right to left) Evaluation of the fit (RANSAC). Strain is computed by differentiating the fitted function

2.5 Strain estimation from the displacement field

The estimation of local surface strain typically involves two steps (Sutton *et al*. 2009): (i) fitting analytical functions (e.g., quadratic functions) to the estimated local displacement field, and (ii) estimating strain by differentiating the fitted function. This research investigates different implementations of the strain estimation within the two-step framework, and evaluates the performance quantitatively using the PBGM.

The strain estimation steps implemented and compared in this research are listed below:

Patch selection: Two types of patches are tested in this research. The first type is square patch defined on the 3D surface. The size of the patch is set to 10in × 10in, considering that the width of the flange of the horizontal beam is 10in. The second type of patch is defined by the element faces of the finite element model (Fig. 6 left). These patches are used to fit analytical functions to the estimated 3D displacement field.

Function selection: Using the local coordinate system of the selected patch (X, Y), linear, bilinear, and quadratic functions are fitted in this research (Fig. 6 right)

$$U_i = \alpha_0^i + \alpha_1^i X + \alpha_2^i Y \tag{6}$$

$$U_i = \alpha_0^i + \alpha_1^i X + \alpha_2^i Y + \alpha_3^i XY \tag{7}$$

$$U_i = \alpha_0^i + \alpha_1^i X + \alpha_2^i Y + \alpha_3^i XY + \alpha_4^i X^2 + \alpha_5^i Y^2 \tag{8}$$

where U_i $(i = 1,2,3)$ are the three components of the estimated 3D displacement field.

RANSAC: The RANSAC algorithm (Fischler and Bolles 1981) is implemented in this research to estimate the strain robustly from noisy displacement field. The algorithm tries to remove outliers of the estimated displacement field within the patch by the iterative process (Fig. 6): (i) the algorithm randomly samples points within the patch (50% in this research) and fits a function using the sampled points only, and (ii) evaluate the deviation of all points within the patch from the fitted function. The points where the deviations are less than the predetermined threshold are regarded as inliers, and other points are regarded as outliers. The algorithm repeats (i-ii) multiple times to find the fitted function with the largest number of inliers. A few threshold values are tested in this research.

Function fitting: Using the inliers within each patch, the selected function is fitted to the local displacement field. First, the estimated optical flow at the inlier samples is converted to the 3D displacement field using the adaptive basis assumption, where the first basis vector is computed by the bilinear interpolation of the finite element displacement at the surrounding nodes. Then, the function is fitted to the projected 3D local displacement field by linear least square approach.

Strain estimation: Once the parametric representation of the local 3D displacement field (U_i with $i = 1,2,3$) is obtained by function fitting, the Lagrangian strain tensor can be obtained by differentiating the function analytically. The formulae for computing the Lagrangian strain tensor are available, for example, in (Sutton *et al*. 2009).

2.6 Performance evaluation criteria

One of the appealing properties of the PBGM is the availability of the ground truth displacement and/or strain values from the finite element analysis. Using the ground truth values, this research investigates the following two error criteria to evaluate the expected performance of the measurement plan and post-processing algorithms

$$Raw\ \ error := d_{\text{est}} - d_{\text{true}} \tag{9}$$

$$Error\ \ ratio := \frac{d_{\text{est}} - d_{\text{true}}}{d_{\text{true}}} \tag{10}$$

where d_{est} and d_{true} stands for the estimated and the ground truth values of the quantities (displacement or strain).

The raw error and error ratio are the local criteria evaluated at each nodal location of the associated finite element model. To get an intuition of the global expected performance of the displacement and strain estimation under the given measurement plan, we can create error maps by assigning colors to each node of the finite element model based on the expected raw error and error ratio

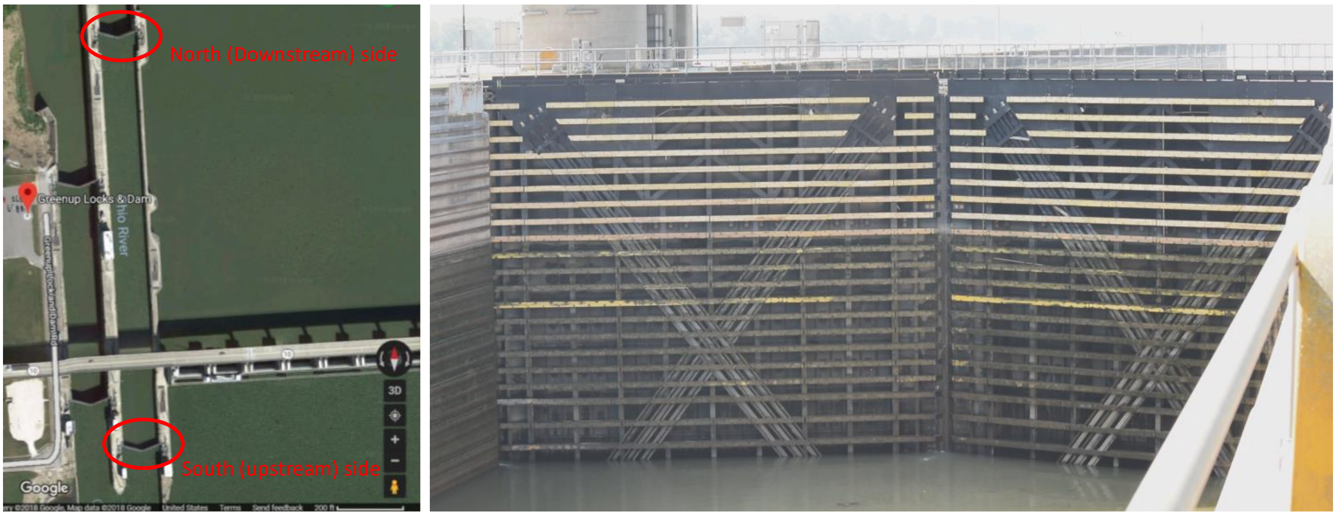

(a) Aerial view (Google Maps) (b) Miter gates (Upstream side)

Fig. 7 Overview of Greenup lock and dam

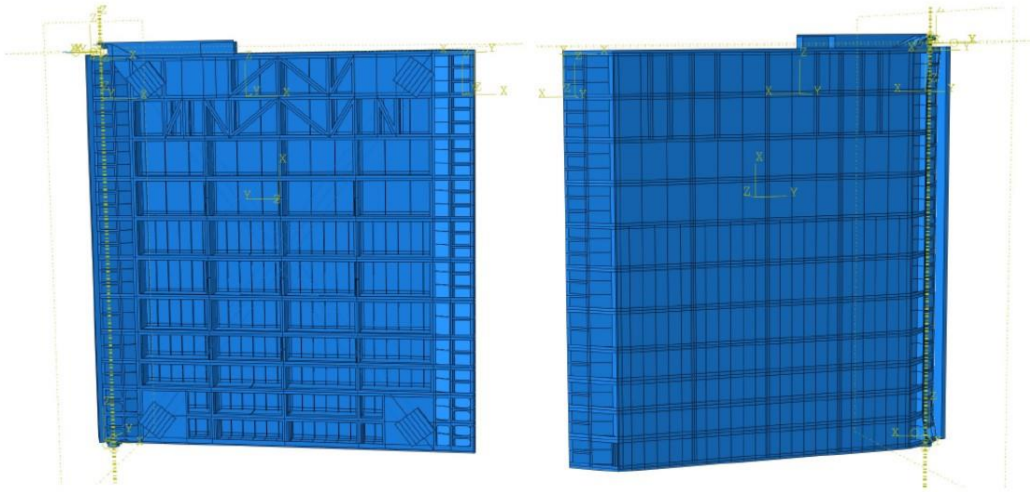

Fig. 8 Overview of finite element model of the Greenup miter gate

values (e.g., Fig. 1(c)). If we have specific regions of interests (ROIs), different measurement plans can be compared quantitatively by computing average values of the evaluation criteria within the ROIs. For the quantitative evaluation of the global performance of the measurement plans with the desired accuracy level, we can count the number of finite element nodes where the raw error or error ratio is below the desired minimum error levels.

3. Results of the proposed framework

This section presents results of the steps of the proposed framework for the vision-based dense displacement and strain measurement. The section first presents the details of the target structure of this research, miter gates of the Greenup lock and dam, followed by the description of the PBGM of the miter gate. Then, the results of dense displacement measurement in the synthetic environment created using the PBGM are presented, with the discussion about the effectiveness of the adaptive basis assumption. Furthermore, the use of the PBGM to optimize the camera location and orientation is demonstrated. Finally, the simulated measurement data is post-processed by the different implementations of the strain estimation algorithms, and the expected performance is compared quantitatively.

3.1 Greenup lock and dam

Greenup lock and dam (US Army Corps of Engineers 2014) is the 11th lock and dam on the Ohio river. The length, width, and lift of the main chamber are 1,200ft, 110ft, and 30ft, respectively. The Greenup lock and dam has two chambers: main chamber and auxiliary chamber, both completed in 1959. This research focuses on the miter gates of the main chamber (Fig. 7), which has the height of 62ft 9in and the transverse length of 61ft 6in.

Structural health monitoring of the Greenup miter gates has been investigated because the gates are instrumented

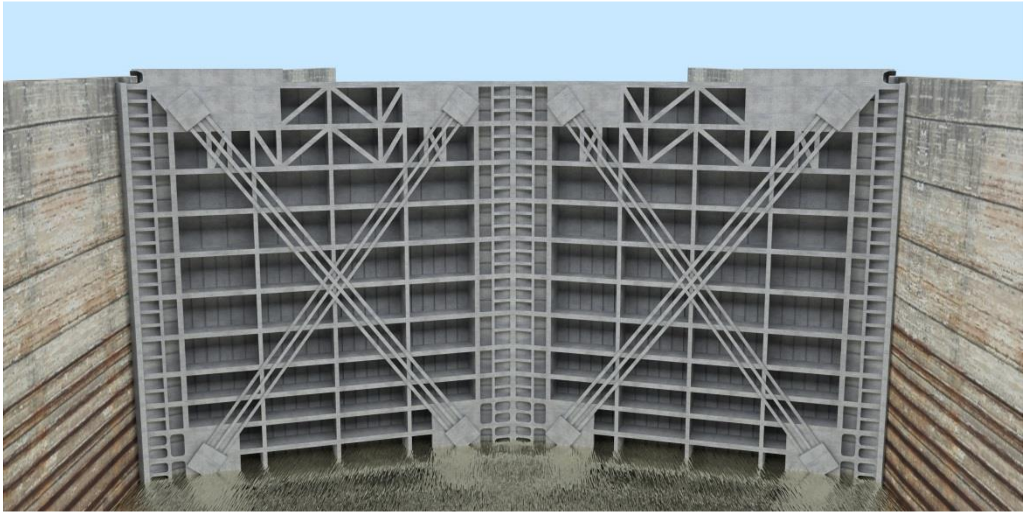

Fig. 9 Overview of the PBGM of the Greenup miter gate

with sensors, such as strain gages and load cells (*SMART Gate*). In (Eick *et al.* 2018, Hoskere *et al.* 2018), an ABAQUS finite element model of the Greenup miter gate was developed, which is used in this research (Fig. 8). The model is made of linear quadrilateral shell elements (S4R), except for the diagonal members modeled by linear beam elements (B31). Contact boundary condition is defined at the quoin following (Hoskere *et al.* 2019). The model has 250,795 nodes and 255,925 elements.

3.2 Physics-based graphics model of the Greenup miter gate

The finite element model of the Greenup miter gate is used to analyze the structural behavior during chamber water level change. In the deformed state, hydrostatic pressure with the zero-pressure height of 600 inches (50 feet) and 240 inches (20 feet) are applied to the upstream and downstream surfaces of the miter gate, respectively. Then, the undeformed and deformed meshes are exported to the Blender for further graphics modeling, where subtle noise texture is added to mimic the steel surface. As discussed previously, the texture is deformed according to the deformed mesh imported from Abaqus. An overview of the PBGM of the Greenup miter gate is shown in Fig. 9.

A camera with the resolution of $4{,}000 \times 2{,}000$ and the focal length of 35 mm is placed at 18 different locations along the top of the left concrete wall of Fig. 9 to simulate the vision-based displacement and strain measurement. The distance along the concrete wall from the camera to the miter end ranges from 100 in to 350 in. The synthetic measurement data is generated by rendering images of the undeformed/deformed structure using the camera.

3.3 Displacement measurement and the performance evaluation

The 3D displacement field is estimated by computing the full field optical flow between images before and after deformation (water level change) and mapping the results to the 3D world coordinate system using the assumptions on the basis vectors. To compare the expected performance of the displacement measurement under different assumptions, images from the camera at 150 in from the gate along the wall are used and the 3D displacement field is estimated.

The maps of the raw error and error ratio criteria evaluated with the first assumption (neglecting vertical displacement) are shown in Fig. 10 with the camera location and orientation. In the figures, blue color indicates negative raw error or low error ratio, and red color indicates positive raw error or high error ratio. Uncolored (black) points are not included in the field of view of the camera. The error ratio in the vertical direction is 1.0 (100%) because the motions in that direction have been neglected by assumption. This assumption is not desirable particularly for the surface strain estimation.

Using the same images of the undeformed/deformed structure, displacement field is estimated again with the second assumption (selecting basis vectors adaptively with the help of finite element analysis results). The maps of the raw error and error ratio are shown in Fig. 11. By defining the subspace adaptively at each part of the structure, the approach can find the better solution, particularly in the direction of relatively small motion (in-plane horizontal and vertical directions).

Note that the actual displacement need not be in the direction of the finite element displacement perfectly, although the perfect match is ideal to get the best accuracy; the first basis vector from the finite element analysis is used to approximate the direction of the actual displacement, and the second basis vector is used to correct the mismatch between the directions of the actual and finite element displacement.

To demonstrate the further capability of the PBGM in evaluating different measurement plans quantitatively, the average values of the error ratio within a region of interest (ROI) shown in Fig. 12(a) are compared among all of the 18 camera locations and orientations (Fig. 12(b)). The second assumption with the adaptive basis vectors is used to convert optical flow results into the 3D displacement. To

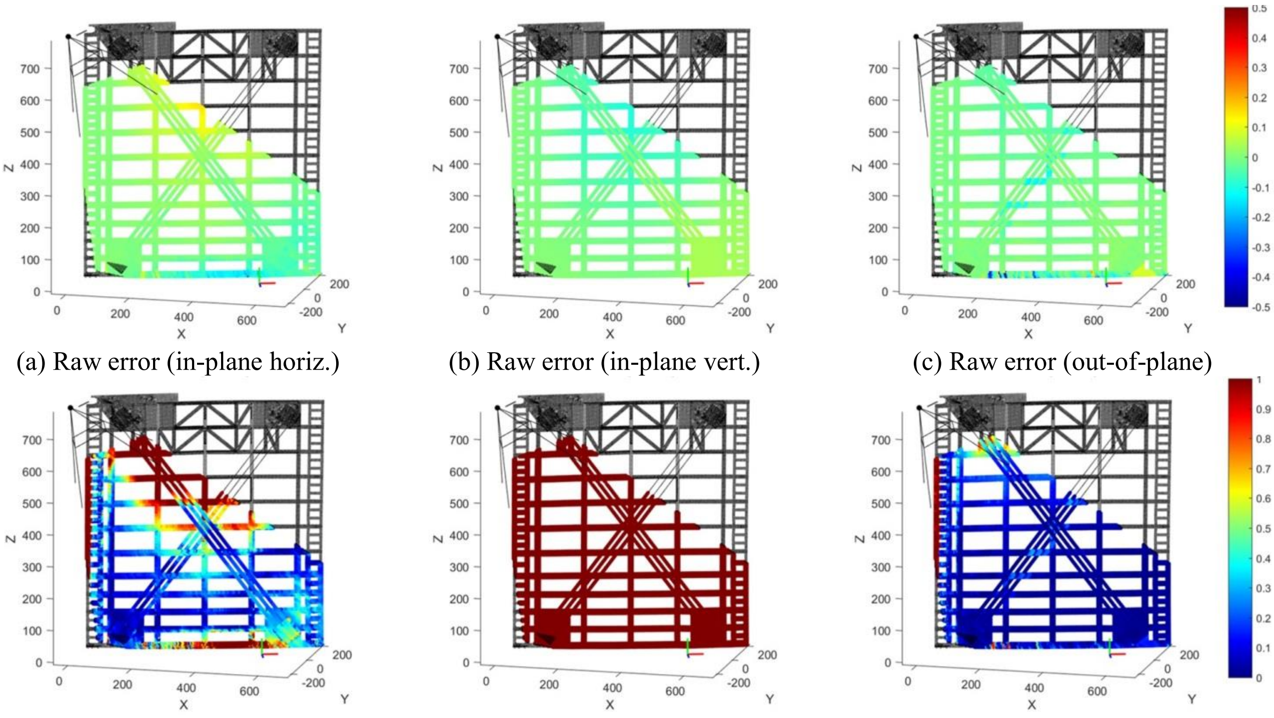

(a) Raw error (in-plane horiz.) (b) Raw error (in-plane vert.) (c) Raw error (out-of-plane)

(d) Error ratio (in-plane horiz.) (e) Error ratio (in-plane vert.) (f) Error ratio (out-of-plane)

Fig. 10 Performance evaluation of displacement estimation with the first assumption (vertical displacement neglected)

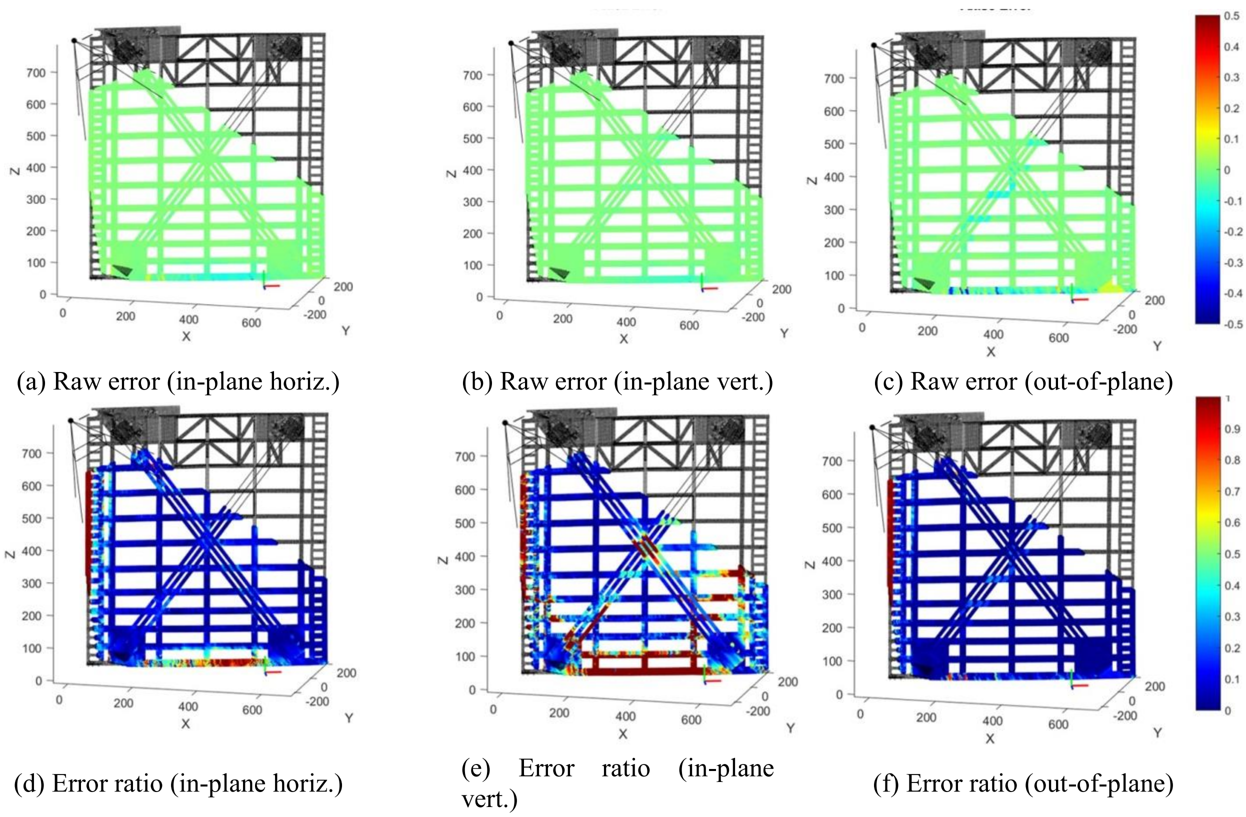

(a) Raw error (in-plane horiz.) (b) Raw error (in-plane vert.) (c) Raw error (out-of-plane)

(d) Error ratio (in-plane horiz.) (e) Error ratio (in-plane vert.) (f) Error ratio (out-of-plane)

Fig. 11 Performance evaluation of displacement estimation with the second assumption (adaptive basis)

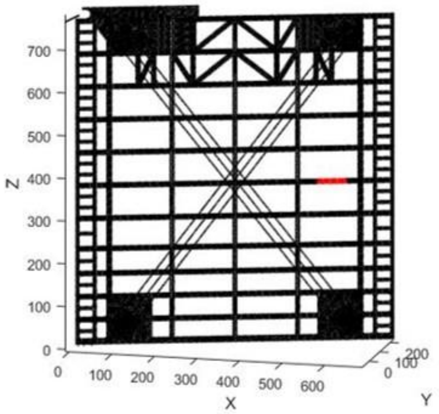

(a) Region of interest

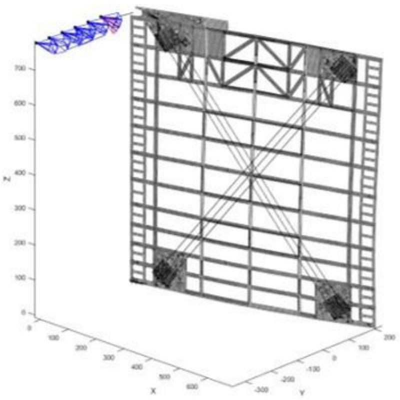

(b) Candidate camera locations/orientations

Fig. 12 Demonstration of camera location/orientation optimization

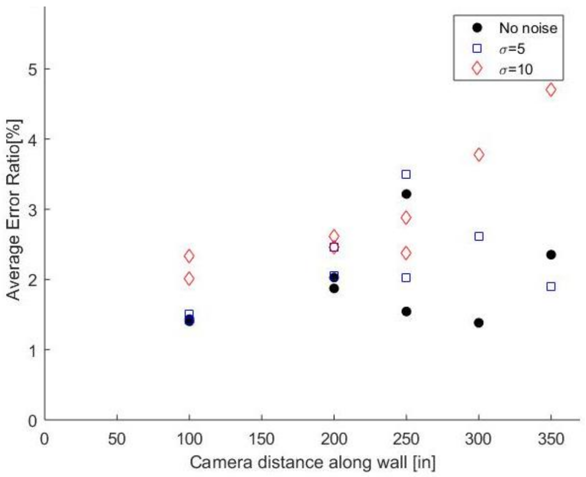

Fig. 13 Average displacement magnitude estimation error ratio within the ROI

mimic the noisy measurement, noise-free images as well as noise-corrupted images (additive Gaussian noise with $\sigma = 5$ and $\sigma = 10$) are evaluated herein. The averaged error ratios between the measured/ground truth displacement magnitude are shown in Fig. 13 for different levels of camera distance along the sidewall. For both the noise-free and noise-corrupted images, the estimated displacement estimation errors are less than 5%. The general trends are: the expected performance improves as we go closer to the target surface, and the error increases as the noise level increases. Besides, the figure also shows the sensitivity of the expected performance on the camera angle, even when the camera distance is constant (see the results for camera distance at 250 in). By examining the averaged error ratio within the ROI, the optimal camera location and orientations for the 3D displacement measurement of the ROI is determined as the one at 100 in from the end of the gate (highlighted in Fig. 12(a)). The performance evaluation discussed in this section is effective for the prediction of the performance of different measurement plans (equipment, camera locations/orientations, post-processing algorithms), as well as the optimization of the measurement plan by examining the expected performance.

3.4 Strain estimation and the performance evaluation

As discussed in the previous section, strain field is estimated by fitting parameterized functions to the local displacement field and differentiating the function with respect to the local coordinate system. For the clarity of presentation, this section examines the data from the camera location/orientation used to create Figs. 10 and 11 (150 in from the end of the gate along the concrete sidewall). Note that this camera setting may not be optimal to measure strain fields if we have a specific ROI in mind (e.g. near the miter of the gate). In such cases, steps similar to the evaluation of displacement estimation performance can be taken to optimize the measurement plan for the specific interests.

Instead of considering specifics of the measurement and optimizing the details of the measurement plan, this section evaluates the global criteria to compare the performance of different realizations of the strain estimation algorithms in general. The numbers of finite element nodes where the raw error and error ratio are below the predetermined threshold are counted as explained in the previous section. In this research, the thresholds for the raw error and error ratio are set to 0.0001 and 0.1, respectively.

The results of performance evaluation of strain estimation algorithms with different optional steps are shown in Fig. 14. The figure compares the counts of the nodes with low raw error and error ratio for different patch selection methods (square, elements of the finite element model), function selection (linear, bilinear, quadratic), and RANSAC parameters (no RANSAC, 0.1 and 0.01 pixel error in the image plane for the inlier selection). The figure shows the performance evaluation for the axial strain estimation in the in-plane horizontal direction, and the evaluation of other strain components can also be done similarly if needed. By comparing the counts for different algorithm realizations, the best implementation for this

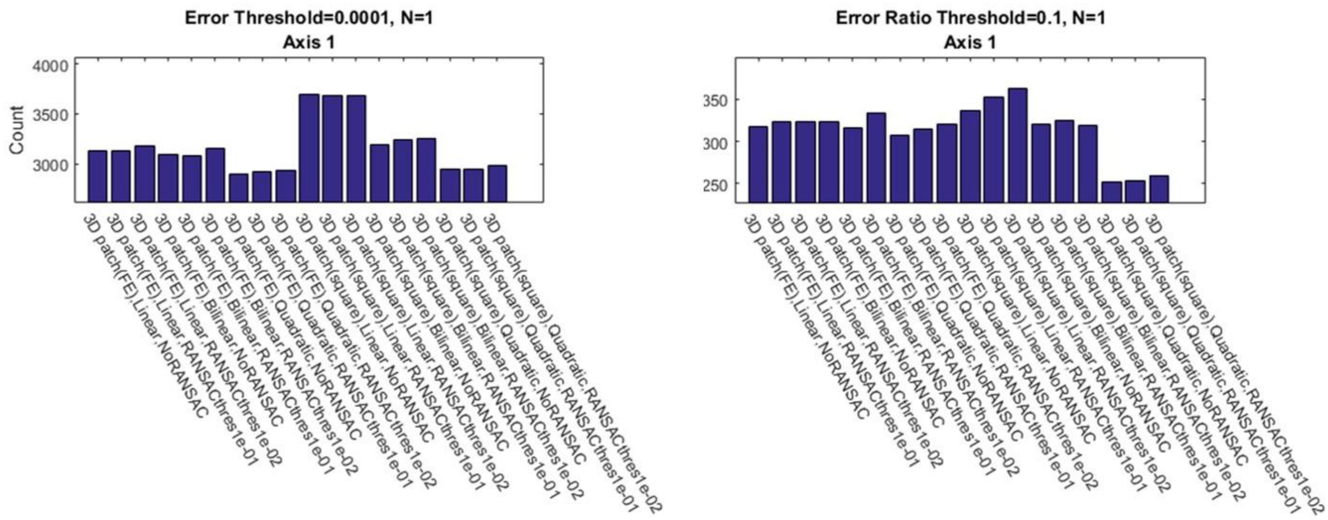

(a) Raw error evaluation (threshold 0.0001) (b) Error ratio evaluation (threshold 0.1)

Fig. 14 Quantitative performance evaluation of different strain estimation methods (axial strain, in-plane horizontal direction)

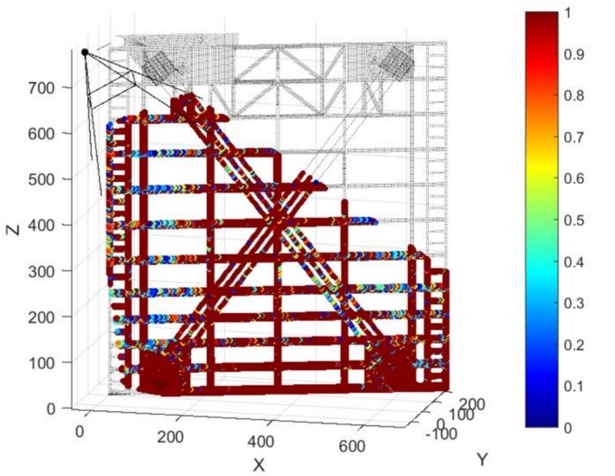

Fig. 15 Map of strain estimation error ratio (axial strain, in-plane horizontal direction)

measurement setting can be determined (Square patch, linear function, and the RANSAC threshold 0.01, if the error ratio is optimized).

As noted previously, even with the optimal post-processing method, the strain estimation becomes increasingly challenging as the camera distance to the target surface increases. The map of the error ratio for the strain estimation in the in-plane horizontal direction are presented in Fig. 15. Compared to the displacement estimation, the region where we can expect accurate strain estimation is significantly smaller, requiring careful planning and optimization to achieve the desired accuracy. The performance evaluation framework proposed in this research is important, because the performance visualization of the framework helps those who carry out measurement avoid spending time in going to the site with a plan which cannot expect desired estimation accuracy.

When the framework implies that the measurement plan at hand needs to be improved to achieve the desired performance, the possible actions are (i) changing the equipment (camera with the higher resolution, lens with larger focal length etc.), (ii) devising a accessing method which enables better camera placement (e.g., UAVs can be used potentially to measure dynamic structural behaviors), (iii) improving the postprocessing steps (e.g., model updating of the finite element model can be performed to investigate the structural behavior through the calibrated model). The significance of the performance evaluation framework proposed in this study is that, every time we come up with a new method for improving the measurement results, we can test the method in the realistic synthetic environment in a labor-efficient and time-effective manner.

4. Conclusions

This study investigates the framework for vision-based dense displacement and strain measurement of miter gates with the quantitative evaluation of the expected performance in the field. The framework consists of the following steps: (i) Estimation of 3D displacement and strain from images before and after deformation (water-fill event), (ii) evaluation of the expected performance of the measurement, and (iii) selection of the measurement setting with the highest expected accuracy. As a testing environment for different measurement settings and post-processing algorithms, the physics-based graphics model (PBGM) of the miter gate at the Greenup Lock and Dam was developed and used effectively. The contributions of this research are listed below:

Physics-based graphics model with consistent texture deformation: The surface texture of the PBGM developed in this research deforms according to the deformation of the mesh obtained by the finite element analysis, which has addressed the challenge of the invalid strain estimation caused by the inconsistent UV mapping.

New approach to convert optical flow estimation results to 3D world coordinate system: Displacement vector obtained by finite element analysis was used to define subspace to which the 2D optical flow results are projected in an adaptive manner (adaptive basis assumption). This approach addresses the problem of conventional conversion approaches, where displacement in one direction is disregarded even if the component is important in some locations of the structure. The synthetic measurement data reveals that the adaptive basis assumption leads to higher accuracy in all three directions, compare to the assumption that the direction with little global displacement is disregarded.

Demonstration of measurement plan optimization based on performance evaluation: Measurement using the PBGM was performed at 18 different camera locations/orientations. The performance of each camera location/orientation was evaluated quantitatively using the average error ratio within a region of interest, from which optimal camera locations and orientations were determined.

Demonstration of post-processing algorithm selection based on performance evaluation: Performance of different methods of converting the estimated displacement field to the strain field were evaluated quantitatively by counting the number of corresponding finite element nodes where expected error ratio is less than the predetermined threshold. By comparing the numbers, the best algorithms and their parameters can be determined for the specific measurement considered.

The dense 3D displacement/strain measurement framework investigated in this research provides quantitative information relevant to structural conditions, as well as the information about the expected quality of the measurement data. The framework leverages the specifics of the measurement appropriately, and therefore can be applied to the planning and/or assessment of every action before/during/after field measurement. This research will contribute to the structural health monitoring of the large number of miter gates of the inland navigation systems by maximizing the time-effectiveness and information gain of the field measurements.

References

Abaqus Scripting User's Guide, http://130.149.89.49:2080/v6.14/books/cmd/default.htm?startat=pt05ch10s11.html

Abaqus Unified FEA - SIMULIA™ by Dassault Systèmes®, https://www.3ds.com/products-ervices/simulia/products/abaqus/

American Society of Civil Engineers (2017), "ASCE's 2017 Infrastructure Report Card: Structurally Deficient Bridges".

Baker, S., Scharstein, D., Lewis, J.P., Roth, S., Black, M.J. and Szeliski, R. (2011), "A database and evaluation methodology for optical flow", *Int. J. Comp. Vision*, **92**(1), 1-31. DOI: 10.1007/s11263-010-0390-2.

Baker, S. and Matthews, I. (2004), "Lucas-kanade 20 years on: a unifying framework", *Int. J. Comp. Vision*. Kluwer Academic Publishers, **56**(3), 221-255. DOI: 10.1023/B:VISI.0000011205.11775.fd.

Barron, J.L., Fleet, D.J. and Beauchemin, S.S. (1994), "Performance of optical flow techniques", *Int. J. Comp. Vision*, **12**(1), 43-77. DOI: 10.1007/BF01420984.

Blender/Python Documentation, https://docs.blender.org/api/2.79/

Blender, https://www.blender.org/

Bruhn, A., Weickert, J. and Schnorr, C. (2005), "Lucas/kanade meets horn/schunck: combining local and global optic flow methods", *Int. J. Comp Vision*, **61**(3), 211-231. DOI: 10.1023/B:VISI.0000045324.43199.43.

Correlated Solutions – VIC-2D, http://correlatedsolutions.com/vic-2d/

Eick, B.A., Treece, Z.R., Spencer, B.F., Smith, M.D., Sweeney, S.C., Alexander, Q.G. and Foltz, S.D. (2018), "Automated damage detection in miter gates of navigation locks", *Struct. Control Health*., **25**(1), e2053. DOI: 10.1002/stc.2053.

Fischler, M.A. and Bolles, R.C. (1981), "Random sample consensus: a paradigm for model fitting with applications to image analysis and automated cartography", *Commun. ACM.*, **24**(6), 381-395. DOI: 10.1145/358669.358692.

Fukuda, Y., Feng, M.Q., Narita, Y., Kaneko, S. and Tanaka, T. (2013), "Vision-based displacement sensor for monitoring dynamic response using robust object search algorithm", *Sensors*, **13**(12), 4725-4732. DOI: 10.1109/JSEN.2013.2273309.

Ghorbani, R., Matta, F. and Sutton, M. (2015), "Full-field deformation measurement and crack mapping on confined masonry walls using digital image correlation", *Exp. Mech.*, **55**(1), 227-243. DOI: 10.1007/s11340-014-9906-y.

GOM Correlate | GOM, https://www.gom.com/3d-software/gom-correlate.html.

Greimann, L., Stecker, J. and Rens, K. (1992), "Inspection and rating of miter lock gates", *J. Perform. Const. Fac.*, **5**(4), 226-238. DOI: 10.1061J(ASCE)0887-3828(1991)5:4(226).

Horn, B.K.P. and Schunck, B.G. (1981), "Determining optical flow", *Artif. Intell.*, **17**(1–3), 185-203. DOI: 10.1016/0004-3702(81)90024-2.

Hoskere, V., Park, J., Yoon, H. and Spencer, B.F. (2018), "Vision-based modal survey of civil infrastructure using unmanned aerial vehicles", *J. Struct. Eng.,* **145**(7), 04019062. DOI: 10.1061/(ASCE)ST.1943-541X.0002321.

Hoskere, V., Eick, B.A., Spencer, B.F., Smith, M.D. and Foltz, S.D. (2019), "Deep bayesian neural networks for damage quantification in miter gates of navigation locks", *Struct. Control Health*.

Hoskere, V., Narazaki, Y. and Spencer, B.F. (2019), "Learning to detect important visual changes for structural inspections using physics-based graphics models", *Int. Conf. Struct. Control Hlth. Intell. Infra*. St. Louis, USA, August.

Hoult, N.A., Andy T.W., Lee, C. and Dutton, M. (2013), "Experimental accuracy of two dimensional strain measurements using Digital Image Correlation", *Eng. Struct.*, **46**, 718-726. DOI: 10.1016/J.ENGSTRUCT.2012.08.018.

Liu, C. (2009), "Beyond pixels: exploring new representations and applications for motion analysis", Doctoral Thesis. Massachusetts Institute of Technology, Cambridge.

Lucas, B.D. and Kanade, T. (1981), "An iterative image registration technique with an application in stereo vision", *Int. Joint Conf. on Artif. Intell.,* Vancouver, August.

Mahal, M. Blanksvard, T., Taljsten, B. and Sas, G. (2015), "Using digital image correlation to evaluate fatigue behavior of strengthened reinforced concrete beams", *Eng. Struct.*, **105**, 277-288. DOI: 10.1016/j.engstruct.2015.10.017.

McCormick, N. and Lord, J. (2012), "Digital image correlation for structural measurements", *Civil Eng.*, **165**(4), 185-190.

Narazaki, Y., Hoskere, V., Spencer, B.F., Foltz, S.D. and Smith, M.D. (2019), "Dense 3D displacement and strain measurement framework of miter gates using computer vision", *Struct. Health. Monit.,* Stanford, CA, USA, September.

Ncorr - Open source 2D digital image correlation MATLAB software,: http://www.ncorr.com/index.php

Pan, B. (2009), "Reliability-guided digital image correlation for image deformation measurement", *Appl. Optics*, **48**(8), 1535. DOI: 10.1364/AO.48.001535.

Pan, B., Qian, K., Xie, H. and Asundi, A. (2009), "Two-dimensional digital image correlation for in-plane displacement and strain measurement: a review", *Meas. Sc. Tech.*, **20**(6), 62001. DOI: 10.1088/0957-0233/20/6/062001.

Pan, B., Tian, L. and Song, X. (2016), "Real-time, non-contact and targetless measurement of vertical deflection of bridges using off-axis digital image correlation", *NDT. E. Int.*, **79**, 73-80. DOI: 10.1016/j.ndteint.2015.12.006.

SMART Gate, https://www.erdc.usace.army.mil/Media/Fact-Sheets/Fact-Sheet-Article-View/Article/476668/smart-gate/

Spencer, B. F., Hoskere, V. and Narazaki, Y. (2019), "Advances in computer vision-based civil infrastructure inspection and monitoring", *Eng.*, **5**(2), 199-222. DOI: 10.1016/J.ENG.2018.11.030.

Sutton, M.A., Orteu, J.J. and Schreier, H.W. (2009), "Image correlation for shape, motion and deformation measurements: basic concepts, theory and applications", Springer Science Business Media.

Szeliski, R. (2011), "Computer vision: algorithms and applications", Springer, New York, NY, USA.

US Army Corps of Engineers (2014), "Lock characteristics general report", Vicksburg, MI, USA.

Wadhwa, N., Rubinstein, M. Durand, F. And Freeman, W.T. (2013), "Phase-based video motion processing", *Trans. Graph.*, **32**(4), 1. DOI: 10.1145/2461912.2461966.

Ye, X.W., Ni, Y.Q., Wai, T.T., Wong, K.Y., Zhang, X.M. and Xu, F. 2013), "A vision-based system for dynamic displacement measurement of long-span bridges: algorithm and verification", *Smart Struct. Sys.*, **12**(4), 363-379. https://doi.org/10.12989/sss.2013.12.3_4.363.

Yoneyama, S., Kitagawa, A., Iwata, S., Tani, K. and Kikuta, H. (2007), "Bridge deflection measurement using digital image correlation", *Exp. Tech.*, **31**(1), 34-40. DOI: 10.1111/j.1747-1567.2006.00132.x.